Advances in Water Resources 133 (2019) 103420

Contents lists available at ScienceDirect

Advances in Water Resources

journal homepage: www.elsevier.com/locate/advwatres

A dynamic pore-network model for spontaneous imbibition in porous media

Chao-Zhong Qin[a,b,c,*], Harald van Brummelen[c]

[a] State Key Laboratory of Coal Mine Disaster Dynamics and Control, Chongqing University, Chongqing 400044, China
[b] School of Resources and Safety Engineering, Chongqing University, Chongqing 400044, China
[c] Department of Mechanical Engineering, Eindhoven University of Technology, The Netherlands

ARTICLE INFO

Keywords:
Spontaneous imbibition
Pore-network model
Porous media
Capillary force
Sharp wetting front
Single-phase imbibition model

ABSTRACT

Spontaneous imbibition in porous media plays a crucial role in many engineering applications such as enhanced oil recovery and geological carbon dioxide storage, in which predicting the imbibition rate is of great importance. In this work, we contribute to developing a novel dynamic pore-network model for spontaneous imbibition in porous media. Multiform idealized pore elements have been used to represent complex pore spaces so that our model bears the potential to quantitatively predict spontaneous imbibition for a 'real' porous medium. A number of case studies have been conducted to test the pore-network model. We show that the capillary force calculated by the Young–Laplace equation is much smaller than that predicted by the pore-network model. The former is usually used to estimate the capillary force at the wetting front in the widely used single-phase imbibition model. We conclude that using the capillary force calculated by the Young–Laplace equation with the mean pore radius notably overestimates the imbibition rate. Moreover, we verify that a sharp wetting front across a few pores is maintained throughout the primary imbibition process, which is in consistence with experimental observations.

1. Introduction

In porous media research, imbibition is the process by which a wetting fluid displaces the defending nonwetting fluid. There are two kinds of imbibition processes, namely, spontaneous imbibition and forced imbibition. Spontaneous imbibition is driven by capillary action, while forced imbibition is driven by an imposed pressure gradient across the media domain. Imbibition is of importance in numerous applications such as enhanced oil recovery (EOR) (Gao et al., 2018; Meng et al., 2017; Morrow and Mason, 2001), capillary trapping in geological carbon dioxide storage (Guo et al., 2016; Valvatne and Blunt, 2004), paper sensors (Elizalde et al., 2015), and inkjet printing (Wijshoff, 2018).

There has been significant research interest in imbibition in porous media. One key topic is to predict the imbibition rate and its dependence on material properties. The imbibition rate yields a crucial performance factor in several applications. For example, in EOR the recovery rate and the extent to which oil is displaced from the matrix are key issues (Morrow and Mason, 2001). In inkjet printing, the imbibition rate of ink needs to be strictly controlled to achieve high printing quality at high throughput.

Spontaneous imbibition of water into a porous medium initially fully filled with air is referred to as wicking. By assuming a sharp wetting front, and neglecting air viscosity and gravity, the penetration depth of liquid water can be given by the single-phase Darcy model:

$$L = \sqrt{\frac{2k^0 p^c}{\varepsilon \mu^w}}\sqrt{t} \tag{1}$$

where ε [-] is the porosity, μ^w [Pa s] is the water dynamic viscosity, k^0 [m^2] is the intrinsic permeability, p^c [Pa] is the capillary pressure, and t [s] is the imbibition time. If the gravity needs to be included and/or the viscosity of the nonwetting phase cannot be neglected, the equation for the penetration depth is presented in Cai et al. (2014), Kunz et al. (2016), Zarandi et al. (2018), which can be analytically or numerically solved. Eq. (1) has been tested for different porous materials such as sandstone (Akin et al., 2000), porous Al_2O_3 (Kuijpers et al., 2017), and glass fiber wicks (Zarandi et al., 2018). Generally, experimental data can be matched by slightly tuning permeability and capillary force, except for cases where a sharp wetting front does not hold any more.

To verify and utilize Eq. (1), however, two fundamental questions still need to be answered: one is how to estimate the capillary force, i.e., p^c in Eq. (1), at the wetting front for a given porous medium; the other is under which conditions the assumption of a sharp wetting front is acceptable. The conditions of interest can be related to material properties, heterogeneity, and the length scale of the domain under consideration. For example, in the late stage of capillary rise in a porous medium, the

* Corresponding author at: State Key Laboratory of Coal Mine Disaster Dynamics and Control, Chongqing University, Chongqing 400044, China.
E-mail address: c.qin@tue.nl (C.-Z. Qin).

https://doi.org/10.1016/j.advwatres.2019.103420
Received 29 March 2019; Received in revised form 8 September 2019; Accepted 10 September 2019
Available online 10 September 2019

flow regime behind the wetting front would switch from single phase to two phase where the sharp wetting front assumption fails (Zarandi and Pillai, 2018). Also, it has been suspected that the sharp front assumption is not acceptable for a thin porous layer. Experimental data of the imbibition rate is very hard to be obtained for thin porous layers, because current measurement techniques have limited spatial and temporal resolution.

To investigate the above issues, pore-scale numerical studies of imbibition in porous media are very useful. Although there are many studies based on direct numerical-simulation models such as VOF (volume of fluid model), SPH (smoothed particle hydrodynamics), LBM (lattice-Boltzmann model), and NSCH (Navier-Stokes-Cahn-Hilliard phase-field models), these studies are generally restricted by excessive computational efforts (Kunz et al., 2018; Raeini et al., 2014; Shokrpour Roudbari et al., 2016). Therefore, usually a small porous medium has been modelled with favorable wettability settings (Kunz et al., 2016; Raeini et al., 2014). Alternatively, dynamic pore-network models can be used which are much more computational efficient. A literature survey shows that most dynamic pore-network models were designed with over-simplified pore elements which cannot represent realistic porous structures (Joekar-Niasar et al., 2010; Qin, 2015; Yin et al., 2018). Although several dynamic pore-network models for two-phase imbibition have been reported (Li et al., 2017; Tørå et al., 2012; Wang et al., 2015), they were developed for simple network structures. In those models, all pore volumes are assigned to pore throats. Phase-mixing is assumed in volumeless pore bodies. It is hard to extend those models to spontaneous imbibition in real porous media.

In this work, we contribute to developing a new dynamic pore-network model for imbibition in porous media. We consider complex pore elements with triangular, square, and circular cross-sections in the model, and therefore enable a more precise description of realistic porous media than previous pore networks. Moreover, the key mechanism of the competition between main terminal meniscus filling and arc menisci filling in a pore body (Ma et al., 1996) has been rigorously implemented, because this mechanism is pivotal in spontaneous imbibition. Multiform pore elements have been widely used in quasi-static pore-network models (Blunt et al., 2013; Oren et al., 1998; Patzek, 2001; Valvatne and Blunt, 2004). In this context, good predictions for capillary pressure and relative permeability were reported. However, its extension to a dynamic pore-network model has remained unexplored.

To test our model, we mainly compare the predictions of the imbibition rate by the pore-network model and by Eq. (1). We show that our PNM can help us verify and improve the single-phase Darcy model for spontaneous imbibition in porous media. The verification of our pore-network model against the VOF- (volume of fluid) based direct numerical simulation model for spontaneous imbibition in a porous medium of sintered glass beads will be presented elsewhere (Qin et al., 2019).

The remainder of the paper is organized as follows. In Section 2, we introduce the pore-network model in detail, including governing equations, constitutive relations, and numerical implementation. In Section 3, we first present a stochastic network generator with predescribed structure information of a porous medium. In addition, the sensitivity of key model parameters to the predicted imbibition rate is discussed. We also conduct case studies to test the developed model. The discussion of model predictions is provided in Section 4, which is followed by main conclusions in Section 5.

2. Pore-network model

In this section, we introduce the dynamic pore-network model for spontaneous imbibition in porous media. Its extension to forced imbibition or drainage processes is straightforward. The main assumptions in our pore-network model are:

- Pore spaces are represented by idealized pore bodies. No volume is affiliated with pore throats (refer to Fig. 1). This is consistent with the concept of watershed used in pore-network extraction (Gostick, 2017).
- Viscous resistances for wetting and nonwetting phases are distributed in both pore bodies and pore throats.
- Wetting and nonwetting phases are incompressible and immiscible.
- The imbibition process is isothermal.

Our pore-network model has been developed specifically for granular porous materials such as soil, sand, and typical sandstones. Therefore, the first model assumption in which we assign all pore volume to pore bodies can be well justified. Our pore-network model is not applicable to porous media with elongated channel-type pores such as shales and nano-porous vycor glass (Gruener et al., 2012). Regarding spontaneous imbibition in those porous media, a more diffusive wetting front occurred and front roughening was amplified. This is because meniscus arrest may occur at asymmetric pore junctions (Sadjadi and Rieger, 2013).

2.1. Governing equations

By virtue of the incompressibility assumption, conservation of mass of the two phases translates into conservation of volume. The volumetric conservation of each phase in a pore body is given as:

$$V_i \frac{d s_i^\alpha}{dt} = -\sum_{j=1}^{N_i} K_{ij}^\alpha \left(p_i^\alpha - p_j^\alpha \right) \quad \alpha = \{n, w\} \tag{2}$$

where i is the pore body index, ij is the pore throat index, n and w indicate the nonwetting and wetting phases, respectively, N_i is the coordination number of pore body i, V [m^3] is the volume, s [-] is the saturation, K [m^3/Pa/s] is the conductivity, and p [Pa] is the pressure. In this work, gravity is neglected.

With the definition of mixture pressure, $\bar{p} = p^n s^n + p^w s^w$, and adding the two conservation equations together (Eq. (2) for the wetting phase and for the nonwetting phase), the pressure equation is derived as (Qin, 2015):

$$\sum_{j=1}^{N_i} \left(K_{ij}^n + K_{ij}^w \right) \left(\bar{p}_i - \bar{p}_j \right) = -\sum_{j=1}^{N_i} \left\{ \left[K_{ij}^n s_i^w - K_{ij}^w \left(1 - s_i^w \right) \right] p_i^c + \left[K_{ij}^w \left(1 - s_j^w \right) - K_{ij}^n s_j^w \right] p_j^c \right\} \tag{3}$$

where the local capillary pressure in pore body i is defined as $p^c = p^n - p^w$. It is seen that in a pore body we solve for both nonwetting and wetting pressures, which are coupled by the capillary pressure under the assumption of local equilibrium.

2.2. Constitutive relations and local physical rules

2.2.1. Idealized pore elements

One of the essential components in the development of a pore-network model is to represent the porous medium of interest with proper idealized pore elements (i.e., pore bodies and pore throats). The choice of idealized pore elements depends on the type of flow and transport process under study (Qin et al., 2016). Further, constitutive relations and local physical rules are dependent on the used idealized pore elements. Here, three types of straight tubes of constant cross-section, as shown in Fig. 2, are employed to approximate complex porous structures, namely, tubes with triangular cross-section, tubes with square cross-section, and tubes with circular cross-section.

A triangular cross-section (e.g., Fig. 2a) can be described by the inscribed circle radius R and two corner half angles, β_1, β_2. The third angle follows from $\beta_3 = \pi/2 - \beta_1 - \beta_2$ with the convention of $0 < \beta_1 \le \beta_2 \le \beta_3 < \pi/2$. We follow Mason and Morrow (1991)'s 'shape factor' definition as:

$$G = \frac{A}{P^2} \tag{4}$$

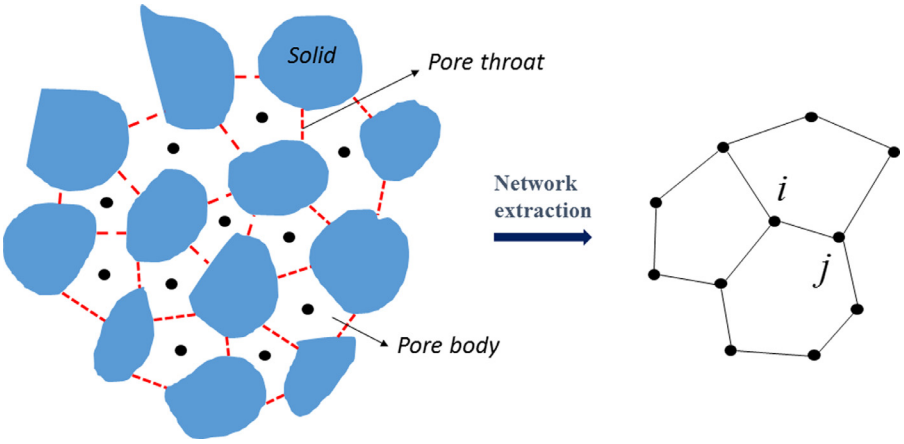

Fig. 1. Schematic of the representation of a porous medium by a pore network. In the left graph, the concept of watershed is used to generate discrete pore spaces, which are connected by pore throats. The right graph shows the extracted pore network composed of idealized pore bodies (i.e., nodes) and pore throats (i.e., bonds).

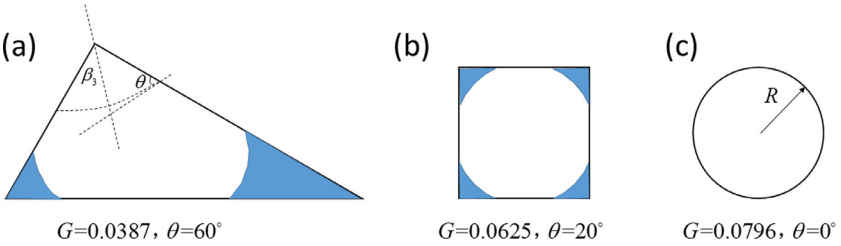

Fig. 2. Schematic of the cross-sections of three idealized pore elements (i.e., pore bodies or pore throats). The blue denotes the wetting phase residing in the corners. θ is the contact angle, and G is the shape factor calculated by Eq. (4).

where A [m^2] is the pore cross-sectional area, and P [m] is the perimeter. For a triangular cross-section, its shape factor and three corner half angles are related as:

$$G = \frac{1}{4}\tan\beta_1 \tan\beta_2 \cot\left(\beta_1 + \beta_2\right) \tag{5}$$

Therefore, by using tubes with triangular cross-section, we can have a range of shape factors from 0 to the maximum value of $\sqrt{3}/36$, the latter corresponding to an equilateral triangle. With the same definition of shape factor, a tube with square cross-section has a shape factor value of 0.0625; and a tube with circular cross-section is characterized by a shape factor value of 0.0796.

In our model, both pore bodies and pore throats are represented by the idealized pore elements described in Fig. 2. However, as mentioned in the first model assumption, no volume is assigned to pore throats. They are mainly used to account for the flow resistance between neighbouring pore bodies. They are not considered in the calibration of porosity. Furthermore, pore-throat sizes are crucial to determine the trapping of nonwetting phase in pore bodies.

2.2.2. Relations of capillary pressure and conductance

The details of calculating pore-body and pore-throat capillary pressure and conductance are presented in Appendix A. In spontaneous imbibition, a pore body exhibits either the main terminal meniscus (MTM) filling or arc menisci (AMs) filling (Ma et al., 1996). As the AMs filling, the snap-off event may be triggered. The used criteria for checking the snap-off is given by Eq. A2 in Appendix A. For a pore body, in the case of the MTM filling, for simplicity the conductance of both nonwetting and wetting phases is approximated by the single-phase conductance given by Eq. (A3), given the fact that its connected pore throats always account for most of the flow resistance.

For a volumeless pore throat, its capillary pressure is approximated by the capillary pressure in its connected upstream pore body. If the MTM filling or the snap-off occurs, the pore throat is fully filled with the wetting phase instantaneously. Otherwise, the pore throat is occupied by both phases. The interface curvature is determined by the capillary pressure. In both cases, the wetting and nonwetting conductance is given in Appendix A.

The flow conductivity from pore body i to pore body j used in Eqs. (2, 3) is calculated as:

$$K_{ij} = 1/\left(\frac{l_i}{2g_i} + \frac{l_j}{2g_j} + \frac{l_{ij}}{g_{ij}}\right) \tag{6}$$

where l is the length [m], and g [m^4/Pa/s] is the conductance. Notice that the superscript α for the phase indicator has been omitted here.

Finally, the following inequality is checked for the existence of corner flow:

$$\beta + \theta < \pi/2 \tag{7}$$

Obviously, for circular pore elements, only the MTM filling is possible. For triangular pore elements, corners may be partially occupied by the wetting phase.

2.2.3. Competition of corner flow and main terminal meniscus movement

In a pore body, the imbibition proceeds via both piston-type displacement (i.e., AMs filling) and the MTM displacement as shown in Fig. 3. The two processes have quite different time scales, which compete each other (Ponomarenko et al., 2011). In the piston type, the wetting phase grows from the corners. At the pore-element-scale, this is much slower than the MTM filling in spontaneous imbibition. The MTM pressure is the same as the entry pressure calculated by equations (A1.1)–(A1.5) based on the MS-P method (Mayer and Stowe, 1965; Princen, 1970, 1969). In our model, if one of the following three conditions is satisfied, the MTM filling of the pore body is active. The first condition is that corner flow is not possible by checking Eq. (7). The second condition is that (a) anyone of its connected pore bodies is with the MTM filling as well as its wetting saturation is larger than 0.5; and (b) the capillary pressure is larger than the MTM pressure. The third condition is that (a) snap off occurs in any of its connected pore bodies; and (b) the capillary pressure is larger than the MTM pressure. Here, the value of 0.5 in the second condition has been selected in the sense of average. Our numerical tests show that the imbibition rate is insensitive to this value for the air-water system. If the sub-pore-scale movement of the MTM is tracked, this empirical value will not be needed. We leave it for a further study.

The same triggering mechanism of the MTM filling applies to a pore throat. On the other hand, when a dry pore body is being invaded and

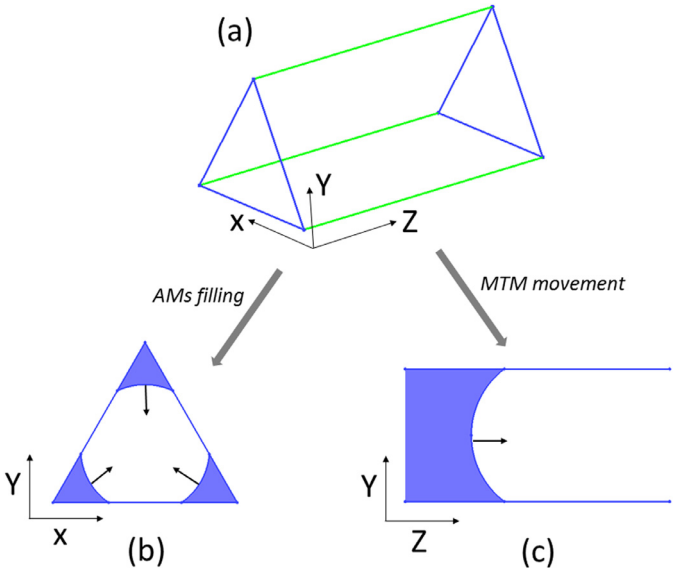

Fig. 3. Schematic of the AMs filling (b) and the MTM movement (c) for a pore body with equilateral triangle cross-section (a). We assume that the wetting phase that accumulates in corners under the AMs filling merges into the MTM when the MTM movement is triggered in a pore body.

the AMs filling is active, a thin pre-wetting film is assumed at corners which corresponds to a capillary pressure value of 10^5 Pa. This value is selected empirically, which may be related to solid surface properties of a porous medium. Fig. 4 shows its effect on the filling rate of a pore body with equilateral triangle cross-section. During the filling, the driving force is the capillary pressure of the swelling menisci. It is seen that the filling time to the snap-off saturation is very sensitive to the assumed pre-wetting film. This is because the initial wetting-phase conductance is determined by the pre-wetting film thickness. If only the AMs filling is used in the model, this parameter is critical to the predicted imbibition rate. But, in spontaneous imbibition, we will show later that the MTM filling is dominant. As a result, this parameter is insensitive to the predicted imbibition rate in our case studies.

Finally, we notice that during the cooperative filling (Blunt, 1997; Oren et al., 1998) of a complex pore body, dynamic variations of capillary pressure are expected. The relation between capillary pressure and saturation depends on both the pore structure and the wetting condition of neighbouring pore bodies. In our model, for an MTM-filling pore body the capillary pressure is assumed to be constant, equal to its MTM entry pressure. However, one may qualitatively account for the cooperative filling by dynamically revising the MTM entry pressure. This aspect will not be further considered in the present study.

2.2.4. Trapping assumption

A natural porous medium usually has a wide distribution of pore sizes. In the imbibition process, small pores are filled relatively fast compared to large pores due to larger suction forces. The magnitude of the difference in the filling speed is closely related to the flow regime of interest. Nonetheless, for a large pore, if its surrounding small pores are filled first, this may cut off the escape pathways of the nonwetting phase in the large pore. In this case, the nonwetting phase is locally trapped. Significant trapping would result in a low saturation value behind the imbibition front.

For an air-water system, several experiments at the mini-column scale have shown that the region behind the imbibition front is almost saturated (Kuijpers et al., 2017; Zarandi et al., 2018). In our pore-network model, without any special treatment of the trapping of nonwetting phase, both imbibition rate and wetting saturation behind the imbibition front will be underestimated. This is because all connected pore throats are marked as the MTM filling once the wetting saturation of a MTM-filling pore body is over 0.5. As mentioned above, the value of 0.5 has been selected in the sense of average. In reality, at the pore scale, phase occupation in a pore throat depends on its location relative to the main meniscus in the pore body. Inclusion of detailed information of pore-throat phase occupation to precluded trapping in pore-network models is non-trivial and a rigorous treatment is beyond the scope of this work. We also tried the remobilization mechanism of the trapped nonwetting phase proposed in (Joekar-niasar and Hassanizadeh, 2012). However, no difference was found when the MTM filling is dominant. In this work, we simply revise the pore-throat gas conductivity as follows. If a pore throat is marked as the MTM filling, its gas conductivity is calculated as:

$$k_{ij}^n = 1/\left(\frac{l_i}{2g_i^n} + \frac{l_j}{2g_j^n} + \frac{l_{ij}}{\nu g_{ij}^n}\right) \tag{8}$$

where g_{ij}^n is equal to the single-phase conductance, and ν is the correction coefficient. ν is set to 1 when both wetting saturation values of its connected pore bodies are smaller than 0.96. This saturation value is the same as that at which the capillary pressure fast approaches zero (see Fig. A2). When the wetting saturation value in either of its connected pore bodies is larger than 0.96, ν is set to zero meaning that this pore throat blocks the transport of the nonwetting phase. Here, the value of 0.96 has been empirically selected in order to (1) make this value close to 1 corresponding to a fully saturated pore body, and (2) match the

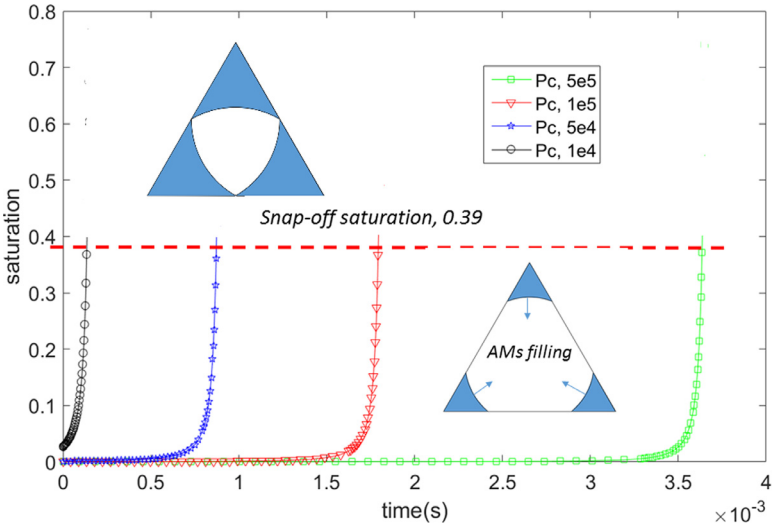

Fig. 4. The effect of the pre-wetting film on the filling rate of a pore body with equilateral triangle cross-section. Only the AMs filling is active. The half corner angle is 30°, and the contact angle is 30° The inscribed radius is 20 μm. The surface tension is 0.073 N/m. The wetting viscosity is 1×10^{-3} Pa s.

wetting saturation behind the wetting front which may be obtained by experiments.

2.3. Numerical implementation

The governing Eqs. (2) and (3) are numerically solved for the primary variables: wetting saturation, s_i^w, and mixture pressure, $\bar{p}_i$. At the end of each time step, the remaining quantities such as capillary pressure and phase conductivity are updated based on the primary variables. The discretization of the governing equations has been elaborated in Qin (2015). In this work, the saturation Eq. (2) is explicitly solved. Although a semi-implicit scheme may stabilize the numerical model, it causes mass imbalance (Joekar-Niasar et al., 2010; Qin, 2015). Further, a first-order differential function of capillary pressure with respect to the wetting saturation needs to be fitted, which is cumbersome for imbibition with complex pore elements.

The local time interval needed to fully drain or fill a pore body is given by:

$$\Delta t_i = \begin{cases} \dfrac{V_i}{q_i^w}\left(1 - s_i^w\right) & for\ local\ imbibition, q_i^w > 0 \\ -\dfrac{V_i}{q_i^w} s_i^w & for\ local\ drainage, q_i^w < 0 \end{cases} \tag{9}$$

where q_i^w [m^3/s] is the total flow rate of the wetting phase in/out pore body i. The standard time step is subsequently obtained as the minimum of the local time intervals. We conducted a sensitivity study of the imbibition rate on the time step. It shows minor influence. This is because in our case studies, the MTM filling is dominant. However, at the late stage of spontaneous imbibition, when the AMs filling plays a role, a large time step may overestimate the imbibition rate due to the used explicit scheme for the saturation equation. In all case studies, we have used half of the minimum of the local time intervals as our time step. Finally, to prevent infinitesimal time-step values, we truncate the wetting saturation in a pore body as follows: when s_i^w is smaller than 10^{-6}, we set $s_i^w = 0$; when $(1 - s_i^w)$ is smaller than 10^{-6}, we set $s_i^w = 1$.

3. Case studies

3.1. Network generation

We generate a three-dimensional pore network representing a homogeneous porous medium by means of the following six-step procedure. First, a given number of pore bodies are generated which have truncated lognormal distributions of inscribed radius, shape factor, and length. Second, conforming to a given porosity value and the total volume of generated pore bodies, the domain dimensions are determined. Third, the ordered pore bodies in size are randomly distributed into the domain in such a manner that overlaps are prevented. Fourth, a pre-described searching length for each pore is used to construct the pore throats. Fifth, an elimination process is conducted: pore throats are randomly eliminated according to a pre-described probability. Sixth, all pore bodies which are not connected with the outlet pores are deleted.

The inscribed radius of a pore-throat size is estimated by:

$$R_{ij} = [\gamma + n(1-\gamma)] \min\left(R_i, R_j\right) \tag{10}$$

where γ is the ratio of pore-throat size to the smaller size of its two connected pore bodies, n is a random number between 0 and 1. The pore-throat length is calculated by:

$$l_{ij} = L_{ij} - R_i^{eq} - R_j^{eq} \tag{11}$$

where L_{ij} is the center distance between the two pore bodies, and R_i^{eq} and R_j^{eq} are the equivalent radii as spherical pore bodies. The pore-throat shape factor is estimated by the average value of its two connected pore bodies. We notice that it may underestimate the permeability of a 'real' porous media by idealized pore bodies. Therefore, we could tune pore-throat lengths to match the permeability given the fact that pore throats are volumeless in our concept of the pore network as illustrated in Fig. 1.

Table 1
Physical parameters and the pore network used in the base case.

Network information	
Domain size	$746 \times 746 \times 746\,\mu m$
The number of pore bodies / pore throats	1194/2672
Porosity	0.4
Permeability	7 Darcy
Mean pore size / standard deviation	20 μm/0.3
Mean coordination number	5.3
The pore-throat ratio, γ	0.2
Physical parameters	
Contact angle	20°
Surface tension	0.073 N/m
Air / water dynamic viscosity	1.83×10^{-5} / 1.0×10^{-3} Pa s
Pre-wetting film capillary pressure	1.0×10^5 Pa
Inlet / outlet reservoir pressure	0/0 Pa

Fig. 5 shows the $10 \times 10 \times 10$ network used in our case studies as well as the pore-size and shape-factor distributions. The network contains 55 pore bodies of square cross-section, 11 ones of circular cross-section, and 934 ones of triangular cross-section. Table 1 presents detailed information of the network in addition to the physical parameters used in the imbibition modeling.

3.2. Sensitivity study of model parameters to the predicted imbibition rate

A few empirical settings are required in the developed pore-network model. Here, we discuss and show the sensitivity study of two main ones: the trapping correction coefficient, ν, in Eq. (8) and the transition function used to force capillary pressure to zero at the end of the MTM filling (Fig. A2). As mentioned in Section 2.2.4, for a pore throat we set ν to zero when the wetting saturation in either of the connected pore bodies is larger than 0.96. This refers to the case studies of 'trapping of air' in this work. On the other hand, it is interesting to test the scenario in which the trapping of air due to the topology of porous structures is neglected. This corresponds to always setting ν to 1. This refers to the case studies of 'no trapping of air'.

The pore network and associated physical parameters listed in Table 1 are used in the sensitivity study. Pressure is set to zero in both inlet wetting and outlet nonwetting reservoirs. When wetting breakthrough occurs, the gradient of capillary pressure is set to zero at the outlet. Initially the network is saturated with the nonwetting phase, i.e., air. Fig. 6a shows the effect of the nonwetting trapping on the imbibition rate. It is seen that the imbibition rate reduces considerably due to the trapping of air, which blocks wetting-phase pathways. At the REV scale, the trapping of air reduces the relative permeability of the wetting phase. At the same time, as expected, the region behind the imbibition front is less saturated in the case of 'trapping of air' as shown in Fig. 6b. Severe trapping of air is found for the used stochastically constructed pore network. However, for a 'real' porous medium its distribution of pores is more or less correlated so that only a small amount of air can be trapped (Qin et al., 2019). Although the stochastically constructed pore network (see Fig. 5) has been used throughout this work, it does not impact our understanding of the developed imbibition model. The modeling of a 'real' porous medium by our pore-network model can be found in Qin et al. (2019).

When a pore body is close to be fully filled by the wetting phase, a transition function is needed to force the capillary pressure to approach zero. Three functions are tested here, which are plotted in Fig. A2. Type 1 is of exponential form. Type 2 has relatively slower switch to zero capillary pressure. Type 3 is of linear form. Fig. 7 shows the influence of the transition function on the predicted imbibition rate for the case with no trapping of air and the case with trapping of air. Overall, the difference of the predicted imbibition rate is minor between Type 1 and Type 2. As expected, a linear transition (i.e., Type 3) would slow

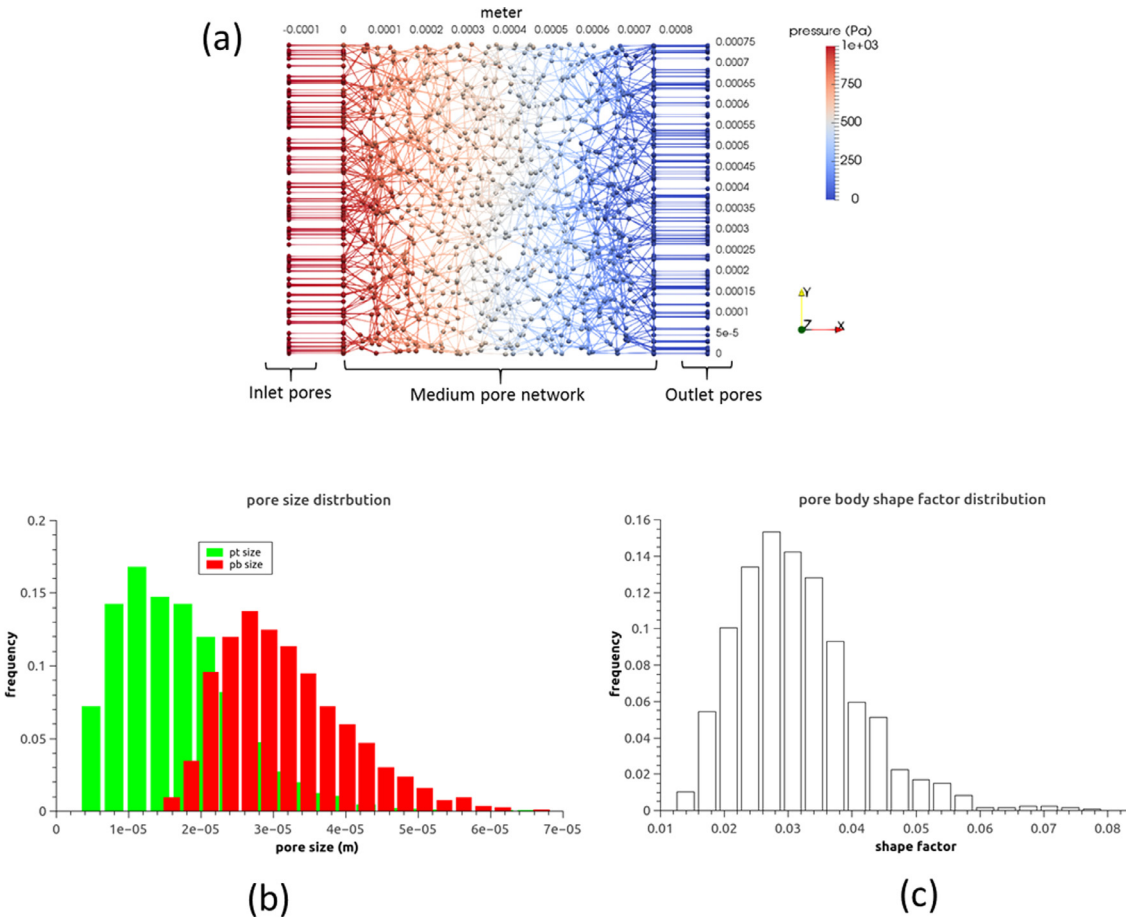

Fig. 5. (a) The $10 \times 10 \times 10$ network used in the case studies. The color map shows the single-phase pressure field with the inlet water pressure of 1000 Pa, (b) the distributions of pore-body size, pore-throat size, and (c) the distribution of pore-body shape factor.

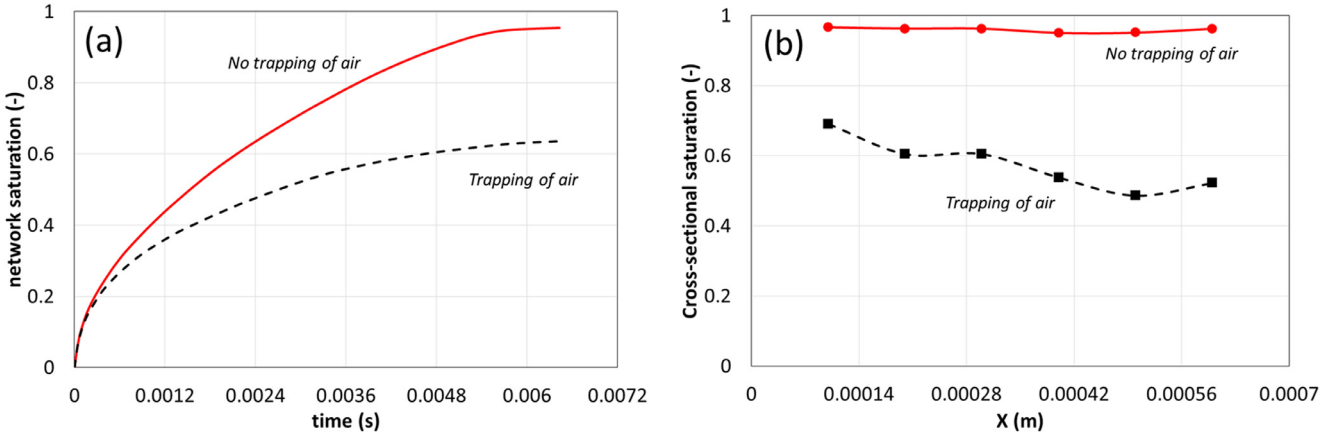

Fig. 6. Sensitivity of the trapping to (a) the predicted imbibition rate and (b) the cross-sectional water saturation distributions along the flow direction at the network saturation of 0.8. The cross-sectional saturation at each location is calculated by averaging a domain length of 200 μm.

down the imbibition, which is much more pronounced for the case with trapping of air as shown in Fig. 7b.

3.3. Results

In this section, we present the results of the case studies under different static contact angle values and inlet wetting reservoir pressures. The same numerical settings as in the sensitivity study are used. The transition function of type 1 is used. Fig. 8 shows the distribution of slope values for the curve $S/\sqrt{t}$. When no trapping of air is assumed (Fig. 8a), one can observe that the slope increases to a peak value, then decreases a little bit to an average value of around 14. The slope decreases fast in the final stage due to the outlet effect. The slight variation of the slope value is caused by the fact that the network size is not large enough to reach the REV (representative elementary volume). Fig. 8a also conveys that the network saturation is essentially linearly proportional to $\sqrt{t}$, except at the beginning and ending parts. Similar observations hold when considering the trapping of air as shown in Fig. 8b, except that with time the peak slope value continues to decrease to a value of around 7. This indicates that the inlet effect influences a larger domain compared

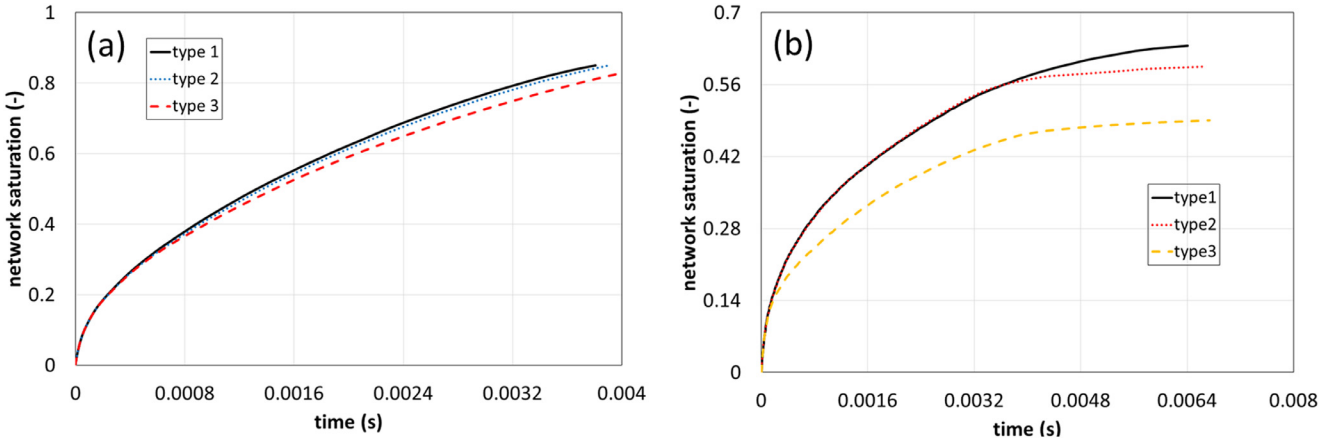

Fig. 7. Influence of the transition function on the predicted imbibition rate for (a) the case with no trapping of air and (b) the case with trapping of air. The function expressions are given and plotted in Fig. A2.

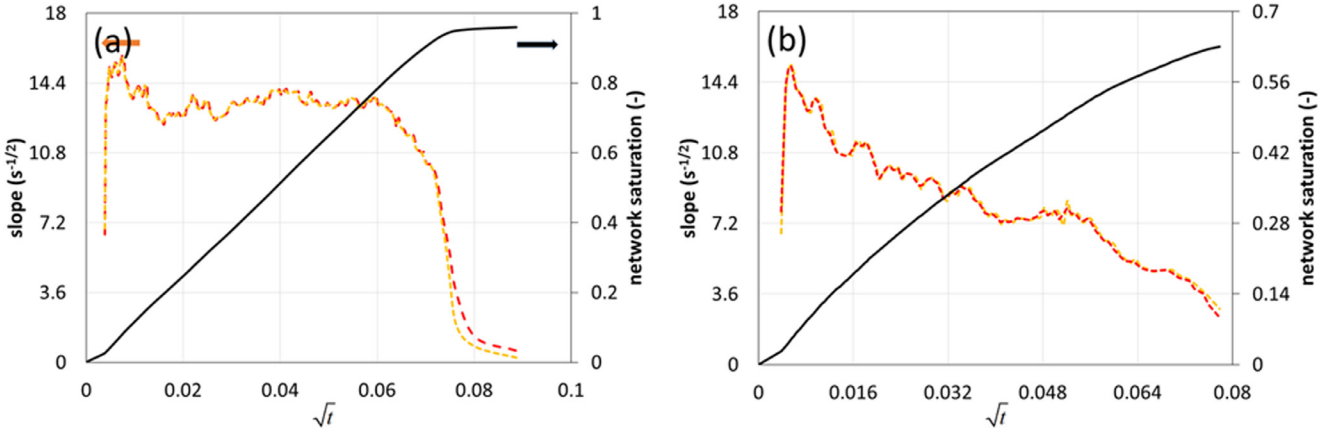

Fig. 8. Distributions of the slope values (i.e., imbibition rate) of the curve $S/\sqrt{t}$ (S is the network saturation), and the network saturation with respect to the square root of imbibition time, for (a) the case with no trapping of air and (b) the case with trapping of air. The static contact angle is 20°, and the inlet wetting reservoir pressure is 0 Pa. The imbibition rate is calculated by both forward and central difference schemes. The difference is indiscernible.

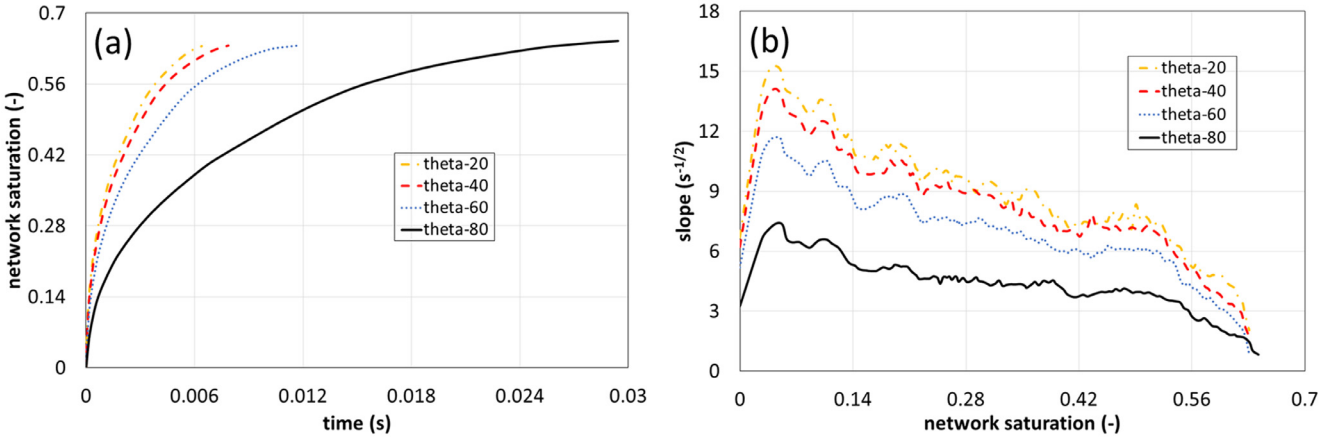

Fig. 9. (a) Effect of the contact angle on the imbibition rate, and (b) the corresponding slope distributions with respect to the network saturation. The trapping of air is considered.

to the case in Fig. 8a. Furthermore, the wetting front needs to travel a much longer distance to reach a constant imbibition rate, which we have confirmed for a larger pore network of $10 \times 10 \times 50$.

Material wettability plays a crucial role in spontaneous imbibition. Such wettability is usually characterized by the static contact angle. For a 'real' porous medium, due to surface roughness and chemical heterogeneity, the advancing and receding contact angle values may considerably deviate from the static one (Forsberg et al., 2010). In this work, we simulate the primary imbibition. Therefore, the contact angle used in our PNM can be regarded as an apparent advancing contact angle. What is more, we assume that any pinning effect due to sharp edges and solid wall roughness at the sub-pore scale can be accounted for by properly revising the contact angle in our model. Our model can in principle handle non-uniform wettability. But, in this work, we restrict our studies to spontaneous imbibition in porous media with uniform wettability.

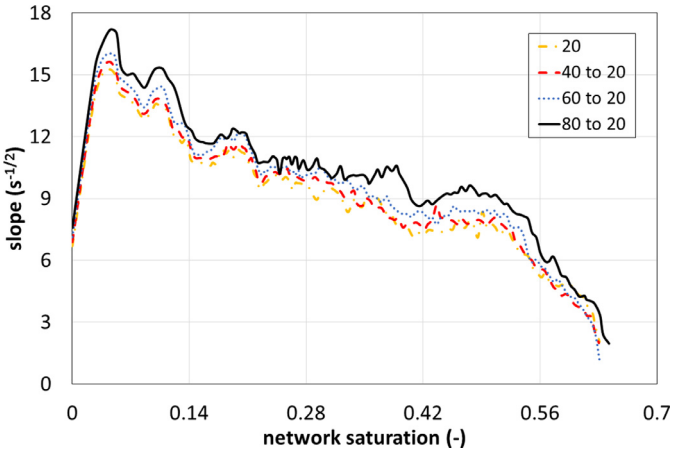

Fig. 10. Distributions of the scaled slope values with respect to the network saturation. For instance, the scaled slope values with the contact angle of 40° is calculated by multiplying the slope values in Fig. 9b by $\sqrt{\cos 40^\circ / \cos 20^\circ}$.

Fig. 9a shows the imbibition rates for four different contact angle values. As expected, the imbibition process slows down considerably with a large contact angle value of 80°. Fig. 9b shows the corresponding slope value distributions with respect to the network saturation. The profiles corresponding to the different contact angle values are very similar in shape. For the single-phase Darcy model (see Eq. (1)), the capillary pressure is usually estimated by the Young–Laplace equation as $p^c = 2\sigma\cos\theta/\bar{R}$ where σ is the surface tension and $\bar{R}$ is the mean pore size. Here, we check if the imbibition rate slope $S/\sqrt{t}$ can be scaled by $\sqrt{\cos\theta}$. In Fig. 10, we scale the slope values with the contact angle values of 40°, 60° and 80° to the case with the contact angle value of 20°. It is seen that the four curves almost overlap. We conclude that under the assumption of uniform wettability, the imbibition rate scales with $\sqrt{\cos\theta}$.

Fig. 11a shows the imbibition rates under three different inlet wetting reservoir pressure values, namely, 2000 Pa, 0 Pa, and −3000 Pa. When a positive pressure value of 2000 Pa of the inlet wetting reservoir is imposed, the imbibition rate is enhanced. The enhancement is slight because the imposed pressure value is much smaller than the suction force of a pore body of the mean pore size, 20 μm. When a relatively small negative pressure value of −3000 is imposed, we see that the imbibition process slows down considerably. This is mainly because large pores with smaller entry capillary pressure than 3000 Pa cannot be invaded by the wetting phase. This case may resemble a late stage of the capillary rise in porous media. Fig. 11b shows the corresponding slope value distributions. It is seen that the three distribution profiles are similar, expect that the medium is least wetted under the inlet pressure of −3000 Pa.

4. Discussion

We have shown the details of the case studies of a small pore network of $10\times10\times10$, which can be seen as part of a thin porous layer (Qin and Hassanizadeh, 2014). For spontaneous imbibition, the saturation slope value behaves relatively constant with different contact angle values. To address the first question of how to estimate the capillary force at the wetting front, here we compare the predictions of the imbibition rate by our PNM and Eq. (1). To use Eq. (1), the assumption of a sharp wetting front should be valid. This will be proved later on for a larger network of $20\times20\times20$. To obtain the temporal network saturation, we reformulate Eq. (1) as follows. With the assumption of a sharp wetting front and an assumed front wetting saturation, S^f, the analytical solution of the network saturation with respect to the square root of the imbibition time is given by:

$$S = \sqrt{\frac{2kp^cS^f}{\varepsilon\mu d^2}}\sqrt{t} \tag{12}$$

where d is the length of the network, and $\sqrt{2kp^cS^f/\varepsilon\mu d^2}$ is the slope. The permeability is approximated by $k = k^0(S^f)^3$. The capillary pressure at the wetting front is approximated by $p^c = 2\sigma\cos\theta/R^m$. When the trapping of air is neglected, with the intrinsic permeability of 7 Darcy calculated by the PNM, and an assumed front saturation value of 0.96, the slope value in Eq. (12) is approximately $19\,s^{-1/2}$. The mean pore size is often used in the calculation of capillary pressure, because it can be obtained by mercury intrusion measurement. If we further consider a pore body with triangular cross-section. Its inscribed radius is equal to R^m. The shape factor is 0.03, which is the mean shape factor of the pore network. For a given contact angle value of 20°, based on 100 realizations of a triangle with the shape factor of 0.03, the effective mean pore radius is obtained as $\tilde{R}^m = 1.216R^m$. It can be used by the Young–Laplace equation to estimate the capillary pressure at the wetting front. Notice that the difference between the mean pore size and the effective one decreases as the increase of the contact angle.

Fig. 12 shows the comparison of the three predicted imbibition curves. It is seen that Eq. (12) notably overestimates the imbibition rate by using either the mean pore size or the effective one. The slope value is overestimated by around 36% when the mean pore size is used. This indicates that the calculation of the capillary pressure with the mean pore size needs to be corrected, in this case by a factor of around 0.54. (i.e.,

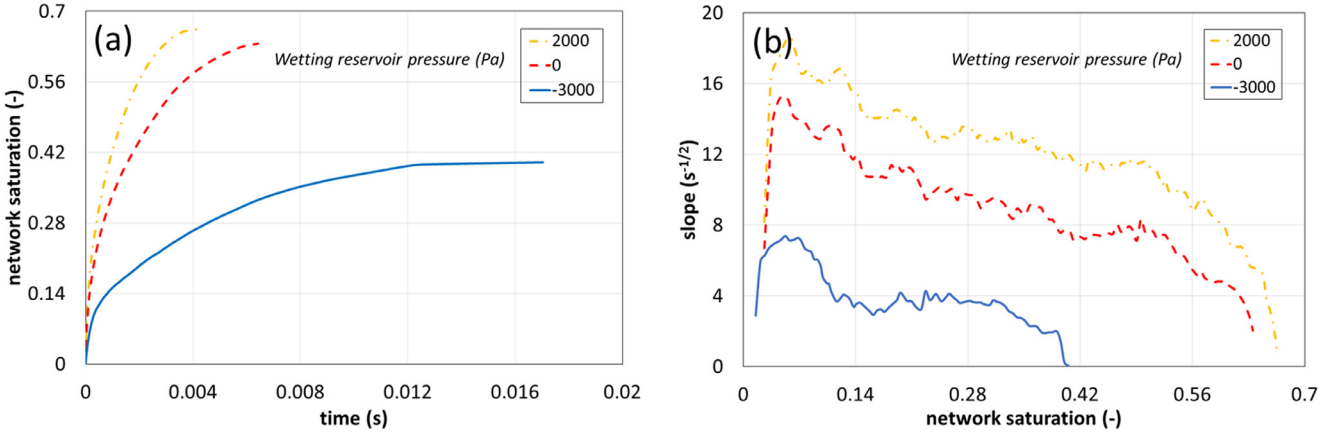

Fig. 11. (a) Imbibition rates and (b) slope value distributions under three different inlet wetting reservoir pressure values, namely, 2000 Pa, 0 Pa, and −3000 Pa. The static contact angle is 20°. The trapping of air is considered.

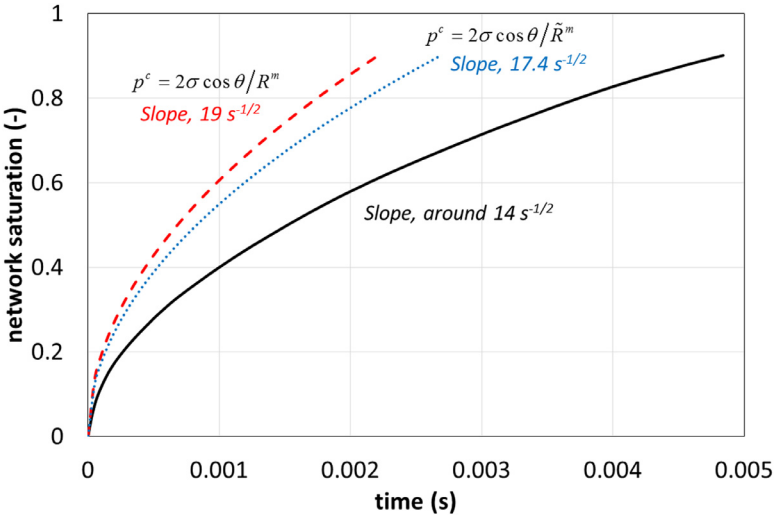

Fig. 12. Comparison of the three imbibition rates predicted by the pore-network model, by Eq. (12) with the mean pore size, R^m, and by Eq. (12) with the effective mean pore size, $\tilde{R}^m$. The static contact angle is 20°.

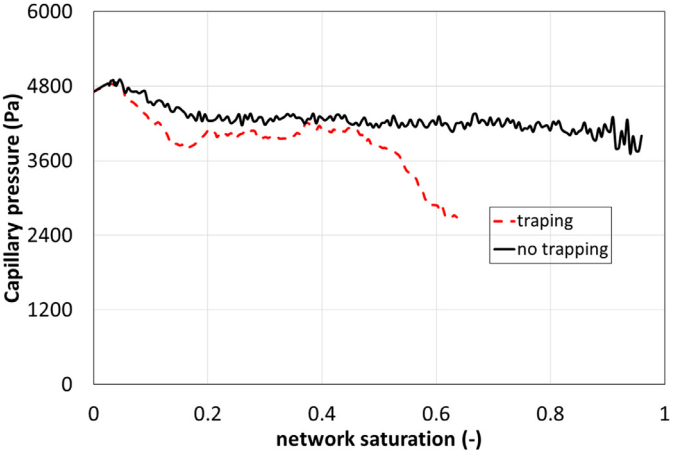

Fig. 13. Capillary pressure versus the network saturation from the pore-network modeling for the case with no trapping of air and the case with trapping of air. The static contact angle is 20°. The capillary pressure is interfacial-area-weighted.

$p^c = 0.54 \times 2\sigma\cos\theta/R^m$). It is expected that this correction factor depends on the pore-size distribution and pore-space topology of a porous medium. By using the effective mean pore size in Eq. (12), the discrepancy from the PNM prediction will be slightly reduced. However, for obtaining the mean shape factor of a porous medium, extensive image analysis needs to be conducted.

Fig. 13 shows the capillary pressure versus the network saturation obtained from the pore-network modeling for the case with no trapping of air and the case with trapping of air. It is seen that the capillary pressure keeps almost constant in both cases. Moreover, trapping of air slightly reduces the capillary pressure. For the case with no trapping of air, the capillary pressure is around 4200 Pa throughout the imbibition process. This again proves that the capillary pressure calculated by the Young–Laplace equation with the mean pore size is drastically overestimated. Moreover, the capillary pressure of 4200 Pa is close to the one of 3704 Pa calculated by $p^c = 0.54 \times 2\sigma\cos\theta/R^m$. The difference between the two values could be attributed to (1) the approximation of water relative permeability and (2) the scale effect (e.g., for the used small network S^f would be overestimated). In reference Zarandi et al. (2018), the authors report that the analytical model over-predicts the wicked height in their capillary rise experiments. However, as time progresses, the model prediction curve asymptotically merges with the experimental points. If one attributes this observation to an overestimated capillary force in their model, it is obvious that the discrepancy decreases as gravity is playing a more and more important role in the capillary rise.

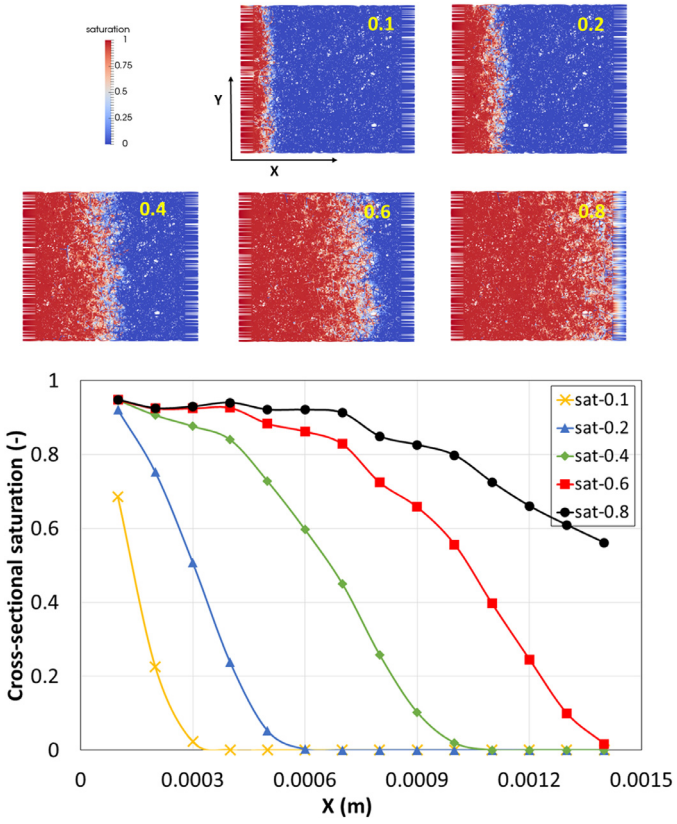

Fig. 14. Snapshots of the imbibition process in a 20 × 20 × 20 network at five different network saturation values. The below graph shows the corresponding distributions of the cross-sectional saturation along the flow direction. The cross-sectional saturation is calculated by averaging a domain size of 200 μm along X.

To verify the assumption of a sharp wetting front, we consider a larger pore network. We simulate the spontaneous imbibition in a 20 × 20 × 20 pore network. The same distribution functions as used in the 10 × 10 × 10 network for pore size, shape factor, and pore length are used. The trapping of air is neglected here. Fig. 14 shows snapshots of water distribution in the network, and the profiles of the cross-sectional

saturation values along the flow direction. The snapshots show that a quite sharp wetting front advances. However, if we define the wetting front by the region where the cross-sectional saturation value is smaller than 0.9, the wetting front (or front roughening) still spans several pores along the flow direction. It is worth noting that our PNM would numerically smear the wetting front to some extent. In other words, the 'real' front would be even sharper than the PNM prediction. Further, the growth of the roughness is indiscernible in Fig. 12. Experimental results (Kuijpers et al., 2017) also show that a sharp wetting front is maintained during the imbibition along significant distances.

Finally, we discuss about further improvements of the present model. First, an advanced trapping model needs to be developed. This is particularly important for highly viscous nonwetting phases such as in a water-oil system. Because the MTM filling is dominant in spontaneous imbibition, the relative positions of pore throats to the connected pore body need to be used to determine the situation of phase occupancy in each pore throat. In other words, details of the MTM movement in a pore body need to be tracked. Second, the cooperative filling of a pore body should be implemented by properly revising the MTM pressure in the pore body.

5. Conclusions

In this work, we have developed a novel dynamic pore-network model (PNM) for spontaneous imbibition in porous media. Complex pore elements are used to represent pore spaces, which allow our model to quantitatively predict a real porous medium. Furthermore, we implement the competition mechanism between the main terminal meniscus (MTM) filling and the arc menisci (AMs) filling of a pore body, which is crucial in spontaneous imbibition. This model enables simulation of a wide range of imbibition processes including versatile settings of boundary conditions and material properties. Our model can be used to efficiently evaluate the imbibition capacity of a porous medium, which may be difficult and expensive to be obtained by experiments.

A number of case studies have been conducted to testify the PNM. We shed light on the estimation of capillary force at the wetting front. We found that the capillary pressure calculated by the Young–Laplace equation with the mean pore size notably overestimates the imbibition rate. For the pore network used in this study, the imbibition rate is overestimated by 36% when air trapping is neglected. We also observed that a sharp wetting front across a few pores maintains and travels through the domain. Under the assumption of uniform wettability, the imbibition rate can scale with $\sqrt{\cos\theta}$ where θ is the static contact angle. Finally, the verification of the present dynamic pore-network model against direct numerical simulations of spontaneous imbibition in a porous medium of sintered glass beads is presented in the follow-up paper (Qin et al., 2019).

Declaration of Competing Interest

We declare that there is no conflict of interest.

Acknowledgements

This research was carried out under project number FIP11 in the framework of Inkjet Research Program FIP: Fundamental Fluid Dynamic Challenges in Inkjet Printing. The support of Océ Technologies within this program is acknowledged. The authors would like to thank Prof. Herman Wijshoff for providing valuable insight into ink absorption into porous substrates, and the anonymous reviewers for their valuable comments.

Supplementary materials

Supplementary material associated with this article can be found, in the online version, at doi:10.1016/j.advwatres.2019.103420.

Appendix A

Relations of capillary pressure and phase conductivities for idealized pore elements

Capillary pressure

There are two imbibition mechanisms (Ma et al., 1996) for a pore body, namely, filling from arc menisci (AMs) and the main terminal meniscus (MTM). For the MTM filling, the capillary pressure (i.e., the entry pressure) will keep constant as the increase of wetting saturation until a pre-set value of saturation is reached. In this work, we set it to 0.96. Then, a transition function of the wetting saturation is used to force the capillary pressure to fast approach zero. Fig. A2 shows three types of functions. The type 1 is primarily used in this work.

The capillary entry pressure during the imbibition is calculated by the following nonlinear equations based on the MS-P theory (Mayer and Stowe, 1965; Patzek, 2001; Princen, 1969):

$$r=\frac{A_{eff}}{L_{nw}+L_{ns}\cos\theta} \tag{A1.1}$$

$$A_{eff}=A-R^2\sum_{i=1}^{n}\left[\frac{\cos\theta\cos\left(\theta+\beta_i\right)}{\sin\beta_i}+\theta+\beta_i-\frac{\pi}{2}\right] \tag{A1.2}$$

$$L_{ns}=\frac{R}{2G}-2\sum_{i=1}^{n}b_i \tag{A1.3}$$

$$L_{nw}=2r\sum_{i=1}^{n}asin\left(\frac{b_i\sin\beta_i}{r}\right) \tag{A1.4}$$

$$b_i=r\frac{\max\left(0,\cos\left(\theta+\beta_i\right)\right)}{\sin\beta_i} \tag{A1.5}$$

where A_{eff} is the cross-sectional area for the nonwetting phase, A is the cross-sectional area of the pore body, L_{nw} and L_{nw} denote the length of nonwetting-wetting interface and the length of nonwetting-wall interface, respectively, and for the remaining notations, one can refer to Fig. A1.

For a pore body with the cross-section of right triangle described in Fig. A1, assuming$R=20\ \mu$m and the surface tension of 0.073 N/m, the obtained entry capillary pressure versus the static contact angle is plotted in Fig. A3a. Also, the corresponding distances, b_1, b_2, and b_3 are plotted. The distances go to zero if corner flow cannot be formed.

For the imbibition filling from AMs, taking the parameters used in Fig. A3a, the capillary pressure versus saturation curves are plotted in Fig. A3b for four contact angle values. Notice that each curve is truncated at its snap-off saturation. The snap-off event is triggered once more than 1 AM touch each other. For a triangle cross-section, we check the following three inequalities:

$$b_1+b_3<l_{A_0C_0} \tag{A2.1}$$

$$b_1+b_2<l_{A_0B_0} \tag{A2.2}$$

$$b_2+b_3<l_{B_0C_0} \tag{A2.3}$$

where l denotes the side length. If one or more are false, the snap-off is triggered. When the snap-off occurs, the nonwetting phase is trapped in the pore body.

As mentioned in Section 2, no volume is assigned to pore throats. The capillary pressure in a pore throat is approximated by the capillary pressure in its connected upstream pore body.

Phase conductance

Flow resistance in both pore bodies and pore throats is taken into account. If a pore is fully filled by either nonwetting or wetting phase, the single-phase conductance is given by Patzek and Kristensen (2001a):

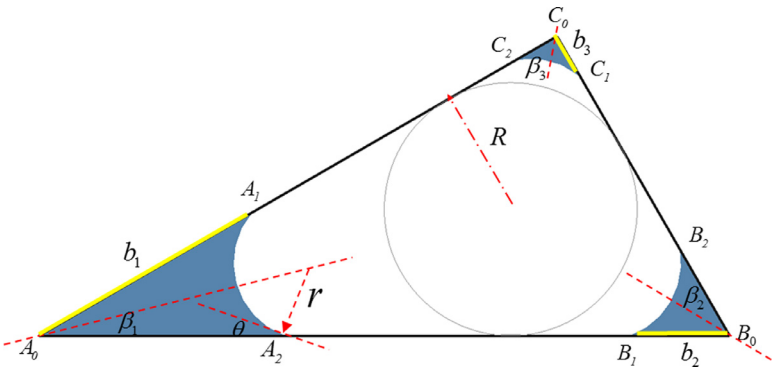

Fig. A1. Wetting phase (in blue) distributions in a pore element, which has a triangular cross-section. The three half corner angles, β_1, β_2, and β_3, are 15°, 30°, and 45°, respectively. θ is the static contact angle, R is the radius of the inscribed circle, r is the radius of the nonwetting-wetting interface curvature, and b denotes the distance from each apex to the corresponding nonwetting-wetting interface along the solid wall (in yellow).

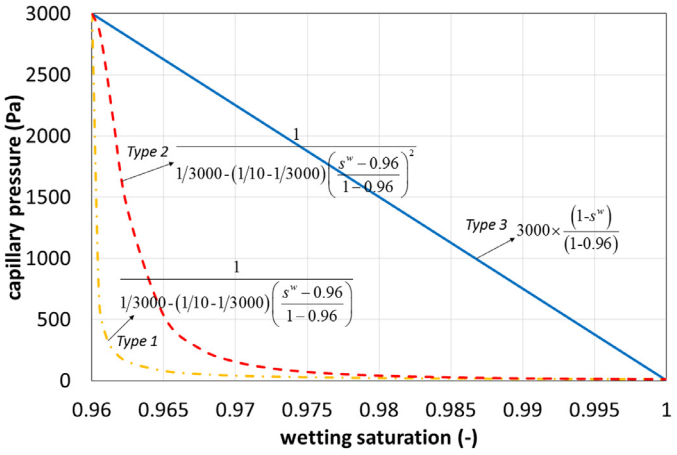

Fig. A2. Three types of transition functions used to force the capillary pressure (3000 Pa) to fast approach zero at the end of the MTM filling.

$$g = \begin{cases} 0.6GS^2 & triangle \\ 0.5632GS^2 & square \\ 0.5GS^2 & circle \end{cases} \tag{A3}$$

where g is the conductance.

If a pore is occupied by both nonwetting and wetting phases, the conductance for wetting phase is calculated as follows. First, for an AM (see Fig. A1), with$b = 1$, the dimensionless corner wetting area is given as (Patzek and Kristensen, 2001b):

$$\tilde{A}^w = \left(\frac{\sin\beta}{\cos(\theta+\beta)}\right)^2 \left(\frac{\cos\theta\cos(\theta+\beta)}{\sin\beta} + \theta + \beta - \frac{\pi}{2}\right) \tag{A4}$$

Further, we define the shape factor for the corner wetting as:

$$\tilde{G}^w = \frac{\tilde{A}^w}{4\left[1-(\theta+\beta-\pi/2)\sin\beta/\cos(\theta+\beta)\right]} \tag{A5}$$

Then, the semi-empirical dimensionless conductance with the perfect slip boundary condition between wetting and nonwetting phases is calculated by Patzek and Kristensen (2001b):

$$\tilde{g}^w = \exp\left\{\left[-18.2066\left(\tilde{G}^w\right)^2 + 5.88287\tilde{G}^w - 0.351809 + 0.02\sin(\beta-\pi/6)\right] / \left(1/4/\pi - \tilde{G}^w\right) + 2\ln S^w\right\} \tag{A6}$$

Finally, the dimensional one is obtained as $g^w = (b^4/\mu)\tilde{g}^w$. Taking the parameters used in Figs. A3 and A4 shows the curves of conductance versus saturation for four contact angle values. Obviously, for the same saturation value, larger contact angle gives larger wetting-phase conductance along the corners. For the nonwetting-phase conductance, it is approximated by:

$$g^n = \begin{cases} 0.6GS^2(1-A^w)^2 & triangle \\ 0.5632GS^2(1-A^w)^2 & square \end{cases} \tag{A7}$$

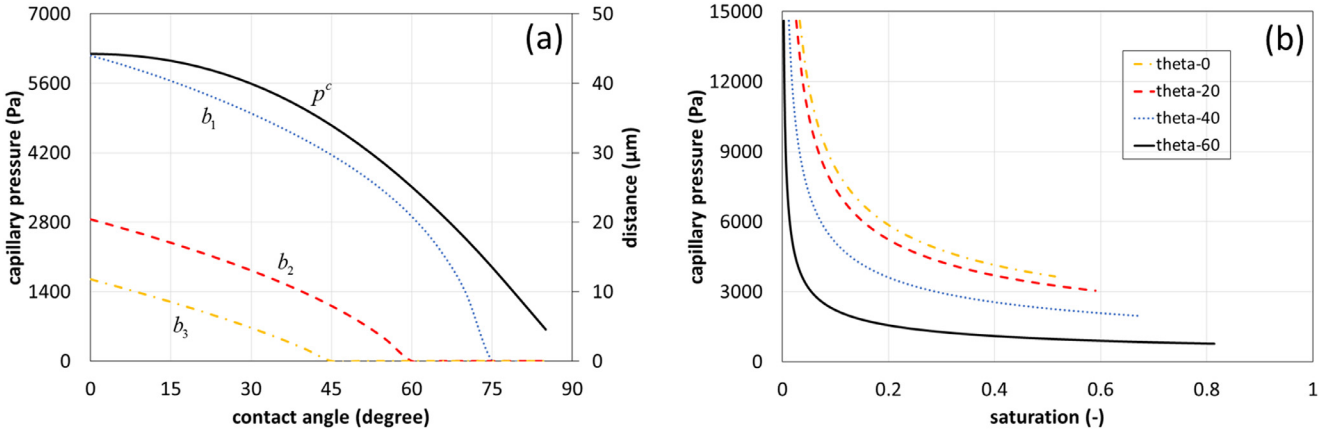

Fig. A3. (a) imbibition entry capillary pressure versus the static contact angle, and the corresponding distances, b_1, b_2, and b_3; (b) the capillary pressure versus the wetting saturation at four different contact angle values for the AMs filling. The cross-section is the right triangle, the inscribed circle radius is 20 μm, and the surface tension is 0.073 N/m.

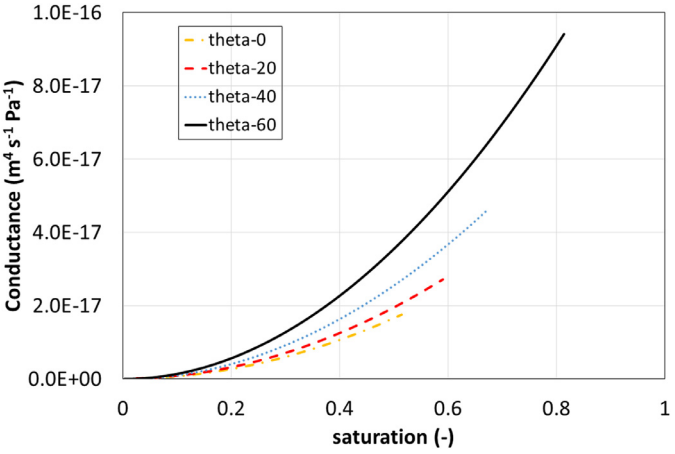

Fig. A4. Wetting-phase conductance versus the wetting saturation for a two-phase occupied pore at four different contact angle values. The cross-section is the right triangle, the inscribed circle radius is 20 μm, and the surface tension is 0.073 N/m.

References

Akin, S., Schembre, J.M., Bhat, S.K., Kovscek, A.R., 2000. Spontaneous imbibition characteristics of diatomite. J. Pet. Sci. Eng. 25, 149–165. https://doi.org/10.1016/S0920-4105(00)00010-3.

Blunt, M.J., 1997. Pore level modeling of the effects of wettability. SPE J 2, 494–508. https://doi.org/10.2118/38435-PA.

Blunt, M.J., Bijeljic, B., Dong, H., Paluszny, A., Pentland, C., Gharbi, O., Mostaghimi, P., Iglauer, S., 2013. Pore-scale imaging and modelling. Adv. Water Resour. 51, 197–216. https://doi.org/10.1016/j.advwatres.2012.03.003.

Cai, J., Perfect, E., Cheng, C.L., Hu, X., 2014. Generalized modeling of spontaneous imbibition based on Hagen–Poiseuille flow in tortuous capillaries with variably shaped apertures. Langmuir 30, 5142–5151. https://doi.org/10.1021/la5007204.

Elizalde, E., Urteaga, R., Berli, C.L.A., 2015. Rational design of capillary-driven flows for paper-based microfluidics. Lab Chip https://doi.org/10.1039/c4lc01487a.

Forsberg, P.S.H., Priest, C., Brinkmann, M., Sedev, R., Ralston, J., 2010. Contact line pinning on microstructured surfaces for liquids in the Wenzel state. Langmuir 26, 860–865. https://doi.org/10.1021/la902296d.

Gao, L., Yang, Z., Shi, Y., 2018. Experimental study on spontaneous imbibition chatacteristics of tight rocks. Adv. Geo-Energy Res. 2, 292–304. https://doi.org/10.26804/ager.2018.03.07.

Gostick, J.T., 2017. Versatile and efficient pore network extraction method using marker-based watershed segmentation. Phys. Rev. E 96, 1–15. https://doi.org/10.1103/PhysRevE.96.023307.

Gruener, S., Sadjadi, Z., Hermes, H.E., Kityk, A.V., Knorr, K., Egelhaaf, S.U., Rieger, H., Huber, P., 2012. Anomalous front broadening during spontaneous imbibition in a matrix with elongated pores. Proc. Natl. Acad. Sci. 109, 10245–10250. https://doi.org/10.1073/pnas.1119352109.

Guo, B., Bandilla, K.W., Nordbotten, J.M., Celia, M.A., Keilegavlen, E., Doster, F., 2016. A multiscale multilayer vertically integrated model with vertical dynamics for CO_2 sequestration in layered geological formations. Water Resour. Res. https://doi.org/10.1002/2016WR018714.

Joekar-niasar, V., Hassanizadeh, S.M., 2012. In: Masoodi Reza, P.K.M. (Ed.), Pore-Network Modeling of Wicking: A Two-Phase Flow Approach. Taylor & Francis Group, pp. 237–262.

Joekar-Niasar, V., Hassanizadeh, S.M., Dahle, H.K., 2010. Non-equilibrium effects in capillarity and interfacial area in two-phase flow: dynamic pore-network modelling. J. Fluid Mech. 655, 38–71. https://doi.org/10.1017/S0022112010000704.

Kuijpers, C.J., Huinink, H.P., Tomozeiu, N., Erich, S.J.F., Adan, O.C.G., 2017. Sorption of water-glycerol mixtures in porous Al2O3 studied with NMR imaging. Chem. Eng. Sci. 173, 218–229. https://doi.org/10.1016/j.ces.2017.07.035.

Kunz, P., Hassanizadeh, S.M., Nieken, U., 2018. A two-phase sph model for dynamic contact angles including fluid–solid interactions at the contact line. Transp. Porous Media 122, 1–25. https://doi.org/10.1007/s11242-018-1002-9.

Kunz, P., Zarikos, I.M., Karadimitriou, N.K., Huber, M., Nieken, U., Hassanizadeh, S.M., 2016. Study of multi-phase flow in porous media: comparison of SPH simulations with micro-model experiments. Transp. Porous Media 114, 581–600. https://doi.org/10.1007/s11242-015-0599-1.

Li, J., McDougall, S.R., Sorbie, K.S., 2017. Dynamic pore-scale network model (PNM) of water imbibition in porous media. Adv. Water Resour. 107, 191–211. https://doi.org/10.1016/j.advwatres.2017.06.017.

Ma, S., Mason, G., Morrow, N.R., 1996. Effect of contact angle on drainage and imbibition in regular polygonal tubes. Colloids Surfaces A Physicochem. Eng. Asp. 117, 273–291. https://doi.org/10.1016/0927-7757(96)03702-8.

Mason, G., Morrow, N.R., 1991. Capillary behavior of a perfectly wetting liquid in irregular triangular tubes. J. Colloid Interface Sci. 141, 262–274. https://doi.org/10.1016/0021-9797(91)90321-X.

Mayer, R.P., Stowe, R.A., 1965. Mercury porosimetry-breakthrough pressure for penetration between packed spheres. J. Colloid Sci. https://doi.org/10.1016/0095-8522(65)90061-9.

Meng, Q., Liu, H., Wang, J., 2017. A critical review on fundamental mechanisms of spontaneous imbibition and the impact of boundary condition, fluid viscosity and wettability. Adv. Geo-Energy Res. 1, 1–17. https://doi.org/10.26804/ager.2017.01.01.

Morrow, N.R., Mason, G., 2001. Recovery of oil by spontaneous imbibition. Curr. Opin. Colloid Interface Sci. 6, 321–337. https://doi.org/10.1016/S1359-0294(01)00100-5.

Oren, P.-.E., Bakke, S., Arntzen, O.J., 1998. Extending predictive capabilities to network models. SPE J 3, 324–336. https://doi.org/10.2118/52052-PA.

Patzek, T.W., 2001. Verification of a complete pore network simulator of drainage and imbibition. SPE J 6, 144–156. https://doi.org/10.2118/71310-PA.

Patzek, T.W., Kristensen, J.G., 2001a. Shape factor correlations of hydraulic conductance in noncircular capillaries: I. One-phase creeping flow. J. Colloid Interface Sci. 236, 295–304. https://doi.org/10.1006/jcis.2000.7414.

Patzek, T.W., Kristensen, J.G., 2001b. Shape factor correlations of hydraulic conductance in noncircular capillaries: II. Two-phase creeping flow. J. Colloid Interface Sci. 236, 305–317. https://doi.org/10.1006/jcis.2000.7414.

Ponomarenko, A., Quéré, D., Clanet, C., 2011. A universal law for capillary rise in corners. J. Fluid Mech. 666, 146–154. https://doi.org/10.1017/S0022112010005276.

Princen, H.M., 1970. Capillary phenomena in assemblies of parallel cylinders. III. Liquid columns between horizontal parallel cylinders. J. Colloid Interface Sci. https://doi.org/10.1016/0021-9797(70)90167-0.

Princen, H.M., 1969. Capillary phenomena in assemblies of parallel cylinders. I. Capillary rise between two cylinders. J. Colloid Interface Sci. https://doi.org/10.1016/0021-9797(69)90379-8.

Qin, C., 2015. Water transport in the gas diffusion layer of a polymer electrolyte fuel cell: dynamic pore-network modeling. J. Electrochem. Soc. 162, F1036–F1046. https://doi.org/10.1149/2.0861509jes.

Qin, C., Hassanizadeh, S.M., Ebigbo, A., 2016. Pore-scale network modeling of microbially induced calcium carbonate precipitation: insight into scale dependence of biogeochemical reaction rates. Water Resour. Res. 52, 8794–8810. https://doi.org/10.1002/2016WR019128.

Qin, C.Z., Hassanizadeh, S.M., 2014. Multiphase flow through multilayers of thin porous media: general balance equations and constitutive relationships for a solid-gas-liquid three-phase system. Int. J. Heat Mass Transf. 70, 693–708. https://doi.org/10.1016/j.ijheatmasstransfer.2013.11.059.

Qin C.Z., van Brummelen H., Hefny M., 2019, Spontaneous imbibition in porous media: verification of a dynamic pore-network model against VoF (volume of fluid)-based direct numerical simulations, Water Resour. Res. (In preparation).

Raeini, A.Q., Blunt, M.J., Bijeljic, B., 2014. Direct simulations of two-phase flow on micro-CT images of porous media and upscaling of pore-scale forces. Adv. Water Resour. 74, 116–126. https://doi.org/10.1016/j.advwatres.2014.08.012.

Sadjadi, Z., Rieger, H., 2013. Scaling theory for spontaneous imbibition in random networks of elongated pores. Phys. Rev. Lett. 110, 1–5. https://doi.org/10.1103/PhysRevLett.110.144502.

Shokrpour Roudbari, M., van Brummelen, E.H., Verhoosel, C.V., 2016. A multiscale diffuse-interface model for two-phase flow in porous media. Comput. Fluids 141, 212–222. https://doi.org/10.1016/j.compfluid.2016.07.006.

Tørå, G., Øren, P.E., Hansen, A., 2012. A dynamic network model for two-phase flow in porous media. Transp. Porous Media 92, 145–164. https://doi.org/10.1007/s11242-011-9895-6.

Valvatne, P.H., Blunt, M.J., 2004. Predictive pore-scale modeling of two-phase flow in mixed wet media. Water Resour. Res. 40, 1–21. https://doi.org/10.1029/2003WR002627.

Wang, Sen, Feng, Q., Dong, Y., Han, X., Wang, Shoulei, 2015. A dynamic pore-scale network model for two-phase imbibition. J. Nat. Gas Sci. Eng. https://doi.org/10.1016/j.jngse.2015.06.005.

Wijshoff, H., 2018. Drop dynamics in the inkjet printing process. Curr. Opin. Colloid Interface Sci. https://doi.org/10.1016/j.cocis.2017.11.004.

Yin, X., Aslannejad, H., de Vries, E.T., Raoof, A., Hassanizadeh, S.M., 2018. Droplet imbibition into paper coating layer: pore-Network modeling simulation. Transp. Porous Media 1–20. https://doi.org/10.1007/s11242-018-1116-0.

Zarandi, M.A.F., Pillai, K.M., 2018. Spontaneous imbibition of liquid in glass fiber wicks, part II: validation of a diffuse-front model. AIChE J 64, 306–315. https://doi.org/10.1002/aic.15856.

Zarandi, M.A.F., Pillai, K.M., Kimmel, A.S., 2018. Spontaneous imbibition of liquids in glass-fiber wicks. part I: usefulness of a sharp-front approach. AIChE J. 64, 294–305. https://doi.org/10.1002/aic.15965.